# Phase-field model coupled with general softening law for cohesive fracture

**Qiao Wang[1,*], Wei Zhou[1], Y.T. Feng[2]**

*[1]State Key Laboratory of Water Resources and Hydropower Engineering Science, Wuhan University, Wuhan 430072, China*

*[2] Zienkiewicz Centre for Computational Engineering, Swansea University, UK*

**Abstract**

Phase-field models have become popular to simulate cohesive failure problems because of their capability of predicting crack initiation and propagation without additional criteria. In this paper, new phase-field damage model coupled with general softening law for cohesive fracture is proposed based on the unified phase-field theory. The commonly used quadratic geometric function in the classical phase-field model is implemented in the proposed model. The modified degradation function related to the failure strength and length scale is used to obtain the length scale insensitive model. Based on the analytical solution of a 1-D case, general softening laws in cohesive zone models can be considered. Parameters in the degradation function can be calibrated according to different softening curves and material properties. Numerical examples show that the results obtained by the proposed model have a good agreement with experimental results and the length scale has a negligible influence on the load-displacement curves in most cases, which cannot be observed in classical phase-field model.

**Keywords**: Phase-field model; general softening law; length scale; cohesive fracture; unified phase-field theory.

## 1. Introduction

The prediction of crack initiation and propagation is a major challenge in solid mechanics. The most known theories or models for fracture mechanics in solids include Griffith's theory [1], linear elastic fracture mechanics (LEFM) [2], and the cohesive zone model (CZM) [3]. These models have been implemented in many numerical methods, such as the finite element method (FEM) [4], the extended finite element method (XFEM) [5, 6], the boundary element method (BEM) [7], the meshless methods [8], the peridynamics [9, 10], the cracking particle method (CPM) [11, 12], the screened Poisson equation [13, 14] and the cellular automaton method [15,

16]. However, some of these methods are not sufficiently efficient to model crack nucleation and propagation, since additional criteria or re-meshing may be needed.

Recently, phase-field models for fracture in solid have attracted attention due to the advantage that the crack initiation and propagation can be predicted automatically. In phase-field models, a new unknown variable, namely the crack *phase-field*, is introduced to regularize the crack surfaces. The discontinuity caused by the crack surfaces is smoothed and the singularity at the crack tip is avoided. The crack propagation or failure can be indicated by the value of the phase-field variable directly without any additional criteria in the whole process. Fixed meshes can be used if the element sizes are fairly small in the zone where the crack is expected to propagate. These advantages make the phase-field models to be easily extended to 3-D models and complex crack patterns like branching, merging and even fragmentation can be handled much more easily than many other methods.

The phase-field models are developed in physics and mechanics communities [17] independently. In physics communities, the models are based on the Landau-Ginzburg phase transition and mainly applied in dynamic analysis [18-23]. In contrast, models proposed in mechanics communities [24, 25] are based on the variational formulation [26] and its regularized form [27] of brittle fracture stems from Griffith's theory. To distinguish between fracture behavior in tension and compression, decomposition methods of the elastic energy density [24, 28, 29] have been proposed to avoid cracking in compression. The initial formulation of phase-field models is for quasi-static problems and can be extended to dynamic analysis [30-36].

The phase-field models have been applied in many areas, such as fractures in thin shells and [37, 38], fracture in heterogeneous structure [39] and hydraulic fracturing [40]. However, most of the models are mainly applied to brittle fracture and only a few models for quasi-brittle [41] or cohesive fracture [42-47] have been proposed. Most of these models cannot consider general softening laws in cohesive zone models. Recently, Wu [41, 48, 49] proposed a unified phase-field theory for quasi-brittle and brittle fracture [50] in solid. In this unified theory, the general softening laws in cohesive zone models can be reproduced accurately by parameter calibration. The classical phase-field model [28] for brittle fracture is a special case of the unified phase-field theory. Besides, the length scale has a negligible influence on the global responses in failure processes [50, 51], which is a very important advantage compared with some other phase-field models since the global responses are highly sensitive to the length scale [52, 53] in these models.

The length scale can be considered as a material parameter [32, 54] in these models, and thus it cannot be chosen arbitrarily; however, a diffusive crack path may be obtained because the length scale is not small enough, while the peak force will be overestimated if a smaller one is chosen [55].

The classical phase-field model with a quadratic geometric crack function $\alpha(s)=s^2$, where $s$ is the crack phase-field, is a particular case of the unified phase-field model [41]. However, its implementation in quasi-brittle or cohesive fracture with general softening laws has not been proposed so far. This paper aims to propose new phase-field damage model coupled with general softening law for cohesive failure based on the unified phase-field theory [41]. In this work, the quadratic geometric crack function $\alpha(s)=s^2$ is considered as in the commonly used classical phase-field model. Similar to the non-standard phase-field model proposed by Wu [41], the phase-field model to be presented below can also consider general softening laws in cohesive zone models, and the length scale also has a negligible influence on the global response in most cases. Although this geometric crack function results in a diffuse crack topology of infinite support, the variational inequality problem [53, 56] can be avoided and the boundedness condition of the phase-field can be ensured automatically, which allows the proposed model to be implemented easily.

This paper is organized as follows. In Section 2, the phase-field model and the unified theory are introduced. Then new phase-field model for cohesive fracture failure are proposed in Section 3, followed by the numerical implementation within the FEM framework in Section 4. Finally, some numerical examples are given in Section 5 to validate the proposed model.

## 2. The phase-field theory for mechanics of damage

### *2.1 The governing equation of the phase-field model*

The regularized energy functional for fracture in the absence of body force can be defined as

$$\prod(\mathbf{u},s)=\int_{\Omega}\psi(\boldsymbol{\varepsilon}(\mathbf{u}))\mathrm{d}\Omega+G_c\int_{\Omega}\gamma(s)\mathrm{d}\Omega-\int_{\partial\Omega}\mathbf{t}\cdot\mathbf{u}\mathrm{d}\partial\Omega \tag{1}$$

with

$$\psi(\boldsymbol{\varepsilon}(\mathbf{u}))=\omega(s)\psi_0(\boldsymbol{\varepsilon}(\mathbf{u})), \tag{2}$$

where $\Omega$ is a bounded domain with boundary $\partial\Omega=\partial\Omega_u\cup\partial\Omega_t$, in which $\partial\Omega_u$ and $\partial\Omega_t$ are the boundaries with prescribed displacement and surface traction, respectively. $\Gamma_c\subset\Omega$ is the crack set, $\mathbf{u}$ is the displacement field, $\mathbf{t}$ is the surface traction, $\boldsymbol{\varepsilon}$ is the strain tensor, $G_c$

is the material fracture toughness or energy, and $\psi_0$ is the energy density function which can be written as

$$\psi_0 = \frac{1}{2}\lambda \mathrm{tr}^2[\boldsymbol{\varepsilon}] + \mu \mathrm{tr}[\boldsymbol{\varepsilon}^2], \tag{3}$$

where $\lambda$ and $\mu$ are the Lame constants. The scalar $s$ is the so called crack phase-field which is a variable to characterize the cracks, $\omega(s)$ is called the degradation function and $\gamma(s)$ is the crack surface density function which satisfies

$$\int_{\Gamma_c} \mathrm{d}\Gamma_c \approx \int_{\Omega} \gamma(s)\mathrm{d}\Omega. \tag{4}$$

The crack initiation and propagation can be automatically tracked by the phase-field $s$. Different degradation functions $\omega(s)$ and crack surface density functions $\gamma(s)$ can lead to different phase-field models. In this section, the unified phase-field theory proposed by Wu [41] is discussed and $\gamma(s)$ is expressed as

$$\gamma(s) = \frac{1}{c_0}\left(\frac{1}{l_0}\alpha(s) + l_0|\nabla s|^2\right), \tag{5}$$

where $l_0$ is the length scale regularizing the crack; while the definitions of $c_0$ and $\alpha(s)$ will be given in Section 2.2.

Now the fracture problem becomes to obtain the displacement and phase-field by solving the minimization problem of energy functional. Based on the variation of functional (1) with respect to the displacement field and phase-field, one can obtain

$$\begin{aligned}\delta\prod(\mathbf{u},s) = &-\int_{\Omega} \mathrm{div}\boldsymbol{\sigma}(\mathbf{u})\cdot\delta\mathbf{u}\mathrm{d}\Omega + \int_{\partial\Omega_t} [\boldsymbol{\sigma}(\mathbf{u})\mathbf{n} - \mathbf{t}]\cdot\delta\mathbf{u}\mathrm{d}\partial\Omega \\ &-\int_{\Omega} \frac{2G_c l_0}{c_0}\nabla^2 s\delta s\mathrm{d}\Omega + \int_{\partial\Omega} \frac{2G_c l_0}{c_0}\frac{\partial s}{\partial \mathbf{n}}\delta s\mathrm{d}\partial\Omega + \int_{\Omega} \left[\frac{G_c}{c_0 l_0}\alpha'(s) + \omega'(s)\psi_0\right]\delta s\mathrm{d}\Omega,\end{aligned} \tag{6}$$

where the divergence theorem is applied. The total energy functional satisfies the unilateral stationary condition [57], i.e., $\delta\prod(\mathbf{u},s) = 0$ for $\delta s > 0$ and $\delta\prod(\mathbf{u},s) > 0$ for $\delta s = 0$, which leads to the governing equation of the problem as [41, 57]

$$\mathrm{div}\boldsymbol{\sigma} = \mathbf{0} \quad \text{on} \quad \Omega, \tag{7}$$

$$\frac{2G_c l_0}{c_0}\nabla^2 s - \frac{G_c}{c_0 l_0}\alpha'(s) - \omega'(s)\psi_0 \le 0, \qquad \delta s \ge 0, \tag{8}$$

where the inequality becomes an equality when $\delta s > 0$ and

$$\boldsymbol{\sigma}(\mathbf{u},s) = \frac{\partial\psi(\boldsymbol{\varepsilon},s)}{\partial\boldsymbol{\varepsilon}}, \tag{9}$$

and the Neumann boundary conditions are

$$\boldsymbol{\sigma}(\mathbf{u})\mathbf{n} = \bar{\mathbf{t}} \quad \text{on} \quad \partial\Omega_t, \tag{10}$$

$$\frac{\partial s}{\partial \mathbf{n}} = 0 \quad \text{on} \quad \partial\Omega, \tag{11}$$

where $\mathbf{n}$ is the unit outward normal of the boundary $\partial\Omega$.

Equation (7) is the balance of linear momentum while Equation (8) is the dissipation inequality.

To distinguish the fracture behavior between tension and compression, a modified energy density function [29] was proposed as follows

$$\psi(\boldsymbol{\varepsilon}(\mathbf{u})) = \omega(s)\psi_0^+(\boldsymbol{\varepsilon}(\mathbf{u})) + \psi_0^-(\boldsymbol{\varepsilon}(\mathbf{u})), \tag{12}$$

where the elastic energy density is decomposed into a tensional part and a compressive part as

$$\psi_0(\boldsymbol{\varepsilon}(\mathbf{u})) = \psi_0^+(\boldsymbol{\varepsilon}(\mathbf{u})) + \psi_0^-(\boldsymbol{\varepsilon}(\mathbf{u})). \tag{13}$$

Some methods for the decomposition of the elastic energy density can be found in [24, 29, 58, 59]. In this paper, the decomposition proposed by Miehe et al. [29] is used.

*2.2 The unified phase-field theory*

In the unified phase-field theory proposed by Wu [41], the degradation function $\omega(s)$ is defined as

$$\omega(s) = \frac{(1-s)^p}{(1-s)^p + Q(s)} = \frac{1}{1+\phi(s)}, \qquad \phi(s) = \frac{Q(s)}{(1-s)^p}, \tag{14}$$

in which $p > 0$, $Q(s) \geq 0$ and

$$Q(s) = a_1 s + a_1 a_2 s^2 + a_1 a_2 a_3 s^3 + \mathrm{L}\ , \tag{15}$$

where $a_i$ are coefficients calibrated from material properties.

The crack surface density function $\gamma(s)$ defined in Equation (5) is applied, in which $\alpha(s)$ and $c_0$ are given as

$$\alpha(s) = \xi_1 s + \xi_2 s^2 + \mathrm{L}\ + \xi_m s^m, \qquad \sum_{i=1}^{m} \xi_i = 1, \tag{16}$$

$$c_0 = 4\int_0^1 \sqrt{\alpha(\beta)}\mathrm{d}\beta, \tag{17}$$

where $l_0$ is the length scale regularizing the crack. From Equation (16), one can have $\alpha(0) = 0$ and $\alpha(1) = 1$, which implies that $s = 0$ represents the undamaged area and that $s = 1$ represents the totally broken area. Equation (17) makes sure that the regularized function (4) represents the crack surface itself. The following quadratic form $\alpha(s)$ is usually used.

$$\alpha(s) = \xi s + (1-\xi)s^2 \tag{18}$$

Then in the unified theory of the 1-D case, the failure strength $f_t$ can be computed by

$$f_t = \sqrt{\frac{2EG_c}{c_0 l_0}\frac{\xi}{a_1}}, \tag{19}$$

where $E$ is the Young's modulus. From Equation (19), the parameter $a_1$ can be obtained as

$$a_1 = \frac{2\xi}{c_0}\frac{l_{ch}}{l_0}, \qquad l_{ch} = \frac{EG_c}{f_t^2}. \tag{20}$$

The parameters $a_2$ and $a_3$ are determined as

$$a_2 = \frac{1}{\xi}[(-\frac{4\pi\xi^2}{c_0}\frac{G_c}{f_t^2}k_0)^{\frac{2}{3}} + 1] - (p-1), \tag{21}$$

$$a_3 = \begin{cases} 0, & p > 2, \\ \dfrac{1}{a_2}[\dfrac{1}{\xi}(\dfrac{c_0 w_c f_t}{2\pi G_c})^2 - (1+a_2)], & p = 2, \end{cases} \tag{22}$$

where $k_0$ is the initial slope, and $w_c$ is the ultimate crack opening. Both $k_0$ and $w_c$ can be determined by softening laws.

Equations (20)-(22) are valid for $\xi \in (0, 2]$ and Wu [41] suggests to use $\xi = 2$. $\xi$ cannot be zero since $\xi = 0$ will obtain a zero failure strength $f_t$ from Equation (19). In Section 3, we will investigate the case $\xi = 0$ and obtain new phase-field model for cohesive fracture, in which the boundedness condition of the phase-field is ensured automatically.

## 3. The new phase-field model for cohesive fracture failure

In this section, new phase-field model for cohesive fracture failure are proposed based on the unified phase-field theory. The crack surface density function used in the classical phase-field model is applied. The 1-D problem is considered and an equivalent cohesive zone model with a general softening curve is used to determine the degradation function $\omega(s)$ for quasi-brittle failure.

### *3.1 The degradation function and crack surface density function*

In the model proposed in this paper, $Q(s)$ in the degradation function is defined as

$$Q(s) = b_2 s^2 P(s) \tag{23}$$

with

$$P(s)=1+b_3 s+b_4 s^2+b_5 s^3+\mathrm{L}\ . \tag{24}$$

In the crack surface density function, $\alpha(s)=s^2$ is used, and $c_0=2$ can be obtained from Equation (8). The model will become the standard or classical phase-field model if $Q(s)=1-(1-s)^2$.

*3.2 Equivalent cohesive zone model*

Consider a bar $x\in[-L,L]$ that is long enough such that the crack evolution is not affected by boundary effects. An increasing displacement $u^*$ is imposed at both ends but along opposite directions to cause a tensile stress in the bar; and the crack initiation is assumed at point $x=0$. From Equation (9), the strain can be evaluated by

$$\varepsilon(s)=\frac{\sigma}{E\omega(s)}=\frac{\sigma}{E}[\phi(s)+1]. \tag{25}$$

Then Equation (8) can be written as [41]

$$\frac{2G_c l_0}{c_0}\nabla^2 s-\frac{G_c}{c_0 l_0}\alpha'(s)+\frac{\sigma^2}{2E}\phi'(s)=0, \tag{26}$$

or, equivalently,

$$\frac{2EG_c}{c_0 l_0}(l_0\nabla s)^2-\frac{2EG_c}{c_0 l_0}\alpha(s)+\sigma^2\phi(s)=0. \tag{27}$$

Assuming $\nabla s=0$ at the symmetric point $x=0$, the stress can be computed as

$$\sigma(s^*)=\sqrt{\frac{2EG_c}{c_0 l_0}\frac{\alpha(s^*)}{\phi(s^*)}}, \tag{28}$$

where $s^*$ is the maximum value of the phase-field at $x=0$, and $s^*=0$ if the crack is just about to initiate at $x=0$.

The failure strength $f_t$ is determined upon the instant of damage initiation, i.e.,

$$f_t=\lim_{s^*\to 0}\sigma(s^*)=\lim_{s^*\to 0}\sqrt{\frac{2EG_c}{c_0 l_0}\frac{\alpha(s^*)}{\phi(s^*)}}=\lim_{s^*\to 0}\sqrt{\frac{2EG_c}{c_0 l_0}\frac{(1-s^*)^p}{b_2 P(s^*)}}=\sqrt{\frac{EG_c}{l_0}\frac{1}{b_2}}, \tag{29}$$

where $c_0=2$ is used. Applying Equation (29), Equation (28) can be written as

$$\sigma(s^*)=\sqrt{\frac{2EG_c}{c_0 l_0}\frac{\alpha(s^*)}{\phi(s^*)}}=\sqrt{\frac{EG_c}{l_0}\frac{(1-s^*)^p}{b_2 P(s^*)}}=f_t\sqrt{\frac{(1-s^*)^p}{P(s^*)}}. \tag{30}$$

The displacement $u^*$ at the point $x=L$ can be evaluated by

$$u^*=\int_0^L\frac{\sigma}{E}[\phi(s)+1]\mathrm{d}x=\frac{\sigma}{E}L+\frac{1}{2}w(\sigma), \tag{31}$$

where $w(\sigma)$ is the apparent displacement jump expressed as

$$w(\sigma)=\frac{2\sigma}{E}\int_0^D \phi(s)\mathrm{d}x. \tag{32}$$

The above equation defines the equivalent cohesive zone model which yields identical global responses to the phase-field model and $D$ is the half bandwidth of the localization band [41]. Finally, Equation (32) can be written as

$$w(s^*)=\frac{2G_c}{f_t}\int_0^{s^*}\left[\frac{P(s^*)}{(1-s^*)^p}-\frac{P(\beta)}{(1-\beta)^p}\right]^{-\frac{1}{2}}\frac{\beta P(\beta)}{(1-\beta)^p}\mathrm{d}\beta. \tag{33}$$

Then the ultimate crack opening $w_c$ with the vanishing stress is determined as

$$w_c=\lim_{s^*\to 1} w(s^*)=\frac{\pi G_c}{f_t}\sqrt{P(1)}\lim_{s^*\to 1}(1-s^*)^{1-p/2}, \tag{34}$$

or, equivalently,

$$w_c=\begin{cases}0, & p<2,\\ \dfrac{\pi G_c}{f_t}\sqrt{P(1)}, & p=2,\\ +\infty, & p>2.\end{cases} \tag{35}$$

Considering both (29) and (35), the parameters $b_i, i>1$ can be determined as

$$b_2=\frac{EG_c}{f_t^2 l_0}=\frac{l_{ch}}{l_0}, \tag{36}$$

$$b_3+b_4+b_5+\mathrm{L}=\begin{cases}0, & p>2,\\ \left(\dfrac{w_c f_t}{\pi G_c}\right)^2-1, & p=2.\end{cases} \tag{37}$$

Equations (30) and (33) indicate that both the stress and the apparent displacement jumps do not depend on the length scale, but depend on the failure strength $f_t$ and the fracture energy $G_c$. However, $f_t$ and $G_c$ are taken as input known material parameters in the proposed model. They do not depend on the length scale, and are used to compute the unknown parameter $b_2$ in Equation (36). Thus the length scale has no influence on the global response.

### *3.3 General softening laws*

The parameters $b_i, i>2$ can be obtained from softening laws. In this paper, the linear and Cornelissen's laws are considered. As discussed above, the length scale $l_0$ has no influence on the softening curves.

#### *3.3.1 Linear softening law*

The linear softening law and the ultimate crack opening $w_c$ are expressed as

$$\sigma(w) = f_t \max(1 - \frac{f_t}{2G_c} w, 0), \qquad w_c = \frac{2G_c}{f_t}. \tag{38}$$

The exponent $p = 2$ should be taken since the value of the ultimate crack opening $w_c$ is finite. Then Equation (37) becomes

$$b_3 + b_4 + b_5 + \mathrm{L} = -0.594715. \tag{39}$$

If only using one parameter $b_3 = -0.594715$, the softening curve is not accurate (see Figure 1). However, one can improve the accuracy by using more parameters from data fitting (see Appendix A). Figure 1 shows that the softening curve using four parameters has a good agreement with the analytical one.

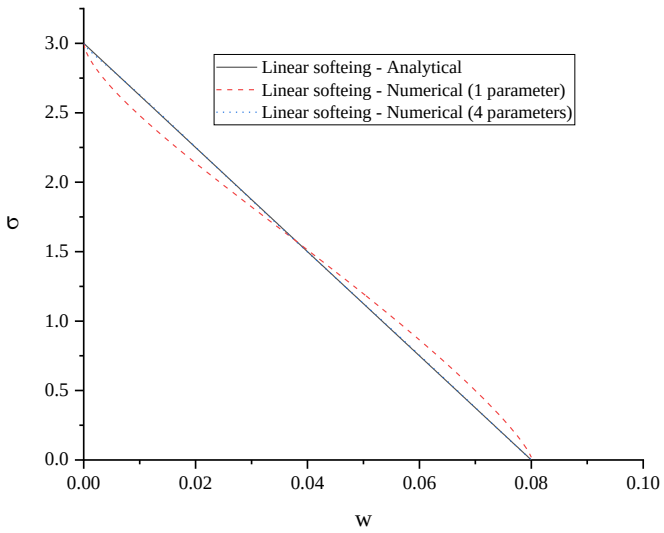


Figure 1. Linear softening curve ($f_t$=3.0MPa, $G_c$=0.12N/mm)

*3.3.2 Cornelissen's softening law*

Cornelissen's softening law [60] for concrete is frequently applied and the softening curve is given as

$$\sigma(w) = f_t[(1.0 + \eta_1^3 r^3)\exp(-\eta_2 r) - r(1.0 + \eta_1^3)\exp(-\eta_2)], \qquad w_c = 5.1361\frac{G_c}{f_t}, \tag{40}$$

where $r = w / w_c$ and $\eta_1 = 3.0$, $\eta_2 = 6.93$ are used for regular concrete. The exponent $p = 2$ and

$$b_3 + b_4 + b_5 + \mathrm{L} = 1.6728. \tag{41}$$

The softening curves for analytical and numerical results with different numbers of parameters are shown in Figure 2. The values of the parameters can be seen in Appendix A.

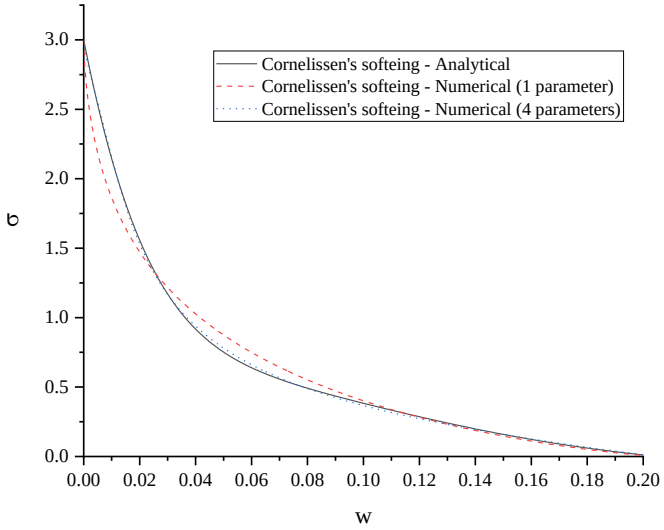


Figure 2. Cornelissen's softening curve ($f_t$=3.0MPa, $G_c$=0.12N/mm)

## 4. Numerical implementation

The finite element method (FEM) is applied to solve the proposed phase-field model with Equations (7) and (8), or ,

$$(\mathbf{u}, s) = \mathrm{Arg}\min\{\int_\Omega \psi(\boldsymbol{\varepsilon}(\mathbf{u}), s)\mathrm{d}\Omega + G_c\int_\Omega \gamma(s)\mathrm{d}\Omega - \int_{\partial\Omega} \mathbf{t}\cdot\mathbf{u}\mathrm{d}\partial\Omega\}. \tag{42}$$

In each load step, either monolithic or staggered algorithm can be employed to compute the unknowns. In this paper, the staggered algorithm described in [28] is applied and two sub-problems controlled by Equations (7) and (8), respectively, are solved alternately. Then the two sub-problems can also be written as two minimization problems by

$$\mathbf{u} = \mathrm{Arg}\min_{\mathbf{u}}\{\int_\Omega \psi(\boldsymbol{\varepsilon}(\mathbf{u}))\mathrm{d}\Omega - \int_{\partial\Omega} \mathbf{t}\cdot\mathbf{u}\mathrm{d}\partial\Omega\}, \tag{43}$$

$$s = \mathrm{Arg}\min_{s}\{\int_\Omega \omega(s)\mathrm{h}\mathrm{d}\Omega + G_c\int_\Omega \gamma(s)\mathrm{d}\Omega\}, \tag{44}$$

where $\mathrm{h}$ is a history-field variable parameter defined as

$$\mathrm{h} = \max\psi_0^+. \tag{45}$$

In Equation (43), the displacement field is solved by fixing the phase-field, while the phase-field is solved in Equation (44) by fixing the displacement field. Iterations between Equations (43) and (44) are performed until the phase-field or displacement field satisfies the prescribed criteria, and this procedure is also known as the alternate minimization algorithm [27].

The staggered algorithm can also be applied without iterations between Equations (43) and (44), and usually much smaller incremental step should be used to obtain accurate results. However, in the phase-field model proposed in this paper, it is found that the algorithm without iterations is normally much more efficient than the algorithm with iterations. Here we only compare the accuracy between these two algorithms in the numerical examples in Section 5, and the efficiency will be investigated systematically in the future.

*4.1 Discretization of Equation (7)*

Equation (7) or Equation (43) can be solved by the standard FEM and the discretization form is

$$\int_{\Omega} \mathbf{B}_u^{\mathrm{T}} \bar{\mathbf{D}} \mathbf{B}_u \mathrm{d}\Omega \hat{\mathbf{u}} = \int_{\partial\Omega} \mathbf{\Phi}_u^{\mathrm{T}} \mathbf{t} \mathrm{d}\partial\Omega, \tag{46}$$

where $\hat{\mathbf{u}}$ are the nodal displacements, $\mathbf{\Phi}_u$ and $\mathbf{B}_u$ are expressed as

$$\mathbf{\Phi}_u = \begin{bmatrix} \Phi^1 & 0 & \Phi^2 & 0 & \mathrm{L} & \Phi^N & 0 \\ 0 & \Phi^1 & 0 & \Phi^2 & \mathrm{L} & 0 & \Phi^N \end{bmatrix}, \tag{47}$$

$$\mathbf{B}_u = \begin{bmatrix} \Phi^1_{,1} & 0 & \Phi^2_{,1} & 0 & \mathrm{L} & \Phi^N_{,1} & 0 \\ 0 & \Phi^1_{,2} & 0 & \Phi^2_{,2} & \mathrm{L} & 0 & \Phi^N_{,2} \\ \Phi^1_{,2} & \Phi^1_{,1} & \Phi^2_{,2} & \Phi^2_{,1} & \mathrm{L} & \Phi^N_{,2} & \Phi^N_{,1} \end{bmatrix}, \tag{48}$$

where $N$ is the total number of nodes, $\Phi^I$ denotes the shape function associated with the $I$ th node, and $\Phi^I_{,j} = \partial\Phi^I / \partial x_j$. $\bar{\mathbf{D}}$ is the degraded constitutive matrix. In this paper, the hybrid model [17] is adopted if not specified otherwise and $\bar{\mathbf{D}}$ is computed as

$$\bar{\mathbf{D}} = \frac{\partial \boldsymbol{\sigma}}{\partial \boldsymbol{\varepsilon}} = \omega(s)\mathbf{D}, \tag{49}$$

where $\mathbf{D}$ is the well-known constitutive matrix in traditional FEM for elasticity problems, and Equation (46) will be a linear system of equations.

*4.2. Discretization of the dissipation inequality*

The phase-field is solved by the dissipation inequality (8) or Equation (44). It should be noted again that there are no inequalities in Equation (8) in the proposed model. By introducing the history field (45), Equation (8) can be rewritten as

$$\frac{2G_c l_0}{c_0} \nabla^2 s - \frac{G_c}{c_0 l_0} \alpha'(s) - \omega'(s)\mathrm{h} = 0. \tag{50}$$

The degradation function $\omega(s)$ used in this paper satisfies $\omega'(0) = \omega'(1) = 0$, i.e., there are two stationary points for $\omega(s)$, where $s = 0$ is the maximum point and $s = 1$ is the

minimum point, and only the minimum point is admissible in the minimization problem. However, it indicates that the undamaged fracture field $s=0$ is always a solution to Equation (50). To avoid the solution $s=0$ for the damaged area, the problem can be reduced to a bound-constrained minimization problem with the bound constraint $s>0$ for the damaged area.

Assuming $\nabla^2 s=0$ when $s=0$, one can obtain the critical failure history field $\mathrm{h}_c$ as

$$\mathrm{h}_c=-\frac{G_c}{c_0 l_0}\frac{\alpha'(0)}{\omega'(0)}=-\frac{G_c}{c_0 l_0}\frac{\alpha''(0)}{\omega''(0)}. \tag{51}$$

Then one can add the bound constraint $s>0$ only when $\mathrm{h}>\mathrm{h}_c$ and set $s=0$ if $\mathrm{h}\le \mathrm{h}_c$.

In this paper, the Barrier method can be applied and Equation (44) can be changed to

$$s=\mathrm{Arg}\min_s\{\int_\Omega \omega(s)\mathrm{h}\mathrm{d}\Omega+G_c\int_\Omega \gamma(s)\mathrm{d}\Omega+\varphi(s)\}, \tag{52}$$

where $\varphi(s)$ is a barrier function and one can choose

$$\varphi(s)=-\frac{1}{t}\int_\Omega \ln s\mathrm{d}\Omega, \tag{53}$$

in which $t$ is a large scalar which should be chosen such that $|\varphi(s)|<\varepsilon$. In this paper, $\varepsilon=10^{-12}$ is applied.

Finally, Equation (52) will result in a non-linear system of equations as

$$\begin{aligned}&\int_\Omega \frac{2G_c l_0}{c_0}\mathbf{B}_s^{\mathrm{T}}\mathbf{B}_s\mathrm{d}\Omega\hat{\mathbf{s}}+\int_\Omega \frac{G_c}{c_0 l_0}\alpha'(s)\mathbf{\Phi}_s^{\mathrm{T}}\mathrm{d}\Omega\\&+\int_\Omega \omega'(s)\mathrm{h}\mathbf{\Phi}_s^{\mathrm{T}}\mathrm{d}\Omega+\frac{1}{t}\int_\Omega \varphi'(s)\mathbf{\Phi}_s^{\mathrm{T}}\mathrm{d}\Omega=0,\end{aligned} \tag{54}$$

where $\hat{\mathbf{s}}$ are the nodal values of the phase-field and

$$\mathbf{\Phi}_s=\begin{bmatrix}\Phi^1 & \Phi^2 & \mathrm{L} & \Phi^N\end{bmatrix}, \tag{55}$$

$$\mathbf{B}_s=\begin{bmatrix}\Phi^1_{,1} & \Phi^2_{,1} & \mathrm{L} & \Phi^N_{,1}\\ \Phi^1_{,2} & \Phi^2_{,2} & \mathrm{L} & \Phi^N_{,2}\end{bmatrix}. \tag{56}$$

Usually, an outer iteration is needed to obtain an appropriate $t$ to ensure that $|\varphi(s)|<\varepsilon$ holds, and then Newton's method is applied in the inner iteration to solve the nonlinear equations. In our computation, the initial guess $t$ is obtained from the value used in the previous load step, and much time will be saved since the number of outer iterations is one in most load steps. The outer iteration will be restarted by choosing a smaller initial $t$ if some values of the phase-field cross the barrier function, i.e. $s<0$ in some iterations. Other methods rather than the Barrier method or other barrier functions can also be applied to solve this minimization problem.

## 5. Numerical examples

In this section, numerical examples are presented to validate the proposed model. If not specified, the plane stress state is assumed for all examples. Linear triangular elements are applied to discretize the domain and the mesh is refined in areas where the crack is expected to propagate. The staggered algorithms with and without iterations are applied to compare the results. No iteration is applied in the classical phase-field model [29].

### *5.1 Single edge notched pure shear test*

In this example, a squared plate with a horizontal notch shown in Figure 3 is tested. The length of the plate is 1.0mm and the vertical displacements on the left and right sides are fixed to zero. The material properties are [29, 50]: Young's modulus $E = 210\times10^3$ MPa, Poisson's ratio $\nu = 0.3$ MPa, failure strength $f_t = 2445.42$ MPa, fracture energy $G_c = 2.7$ N/mm. The staggered algorithm without iterations is applied in this example and the displacement increment is set to $\Delta u = 0.5\times10^{-5}$ mm. In total, 159201 of uniform quadrilateral elements are used to discretize the model and the length scale $l_0 = 0.01$ mm is employed in this example. The linear softening law is used and both the non-hybrid model and the hybrid model [17] are tested.

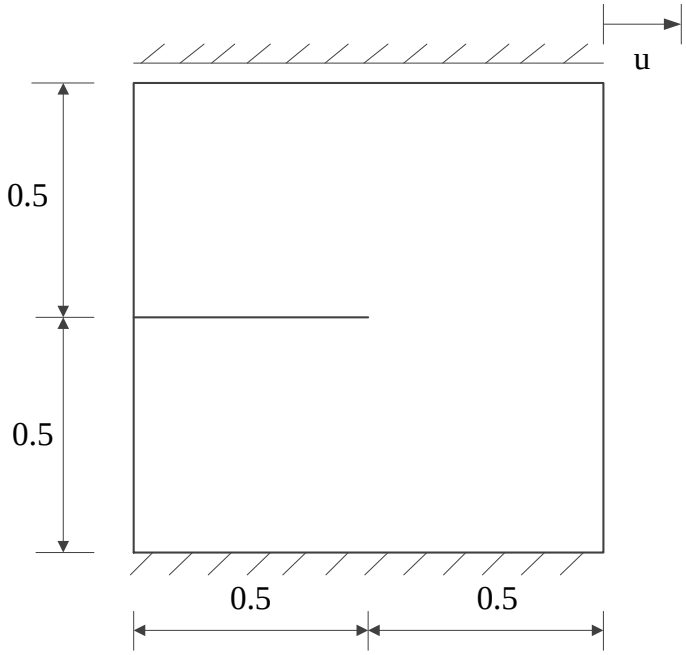


Figure 3. Single edge notched square under pure shear (unit: mm)

The crack-paths obtained by the proposed model with 1 parameter in the degradation function (see Appendix A) are shown in Figure 4. One can observe that the non-hybrid model and the hybrid model can obtain the similar crack path in this example. The load-displacement curves

are shown in Figure 5. The results obtained by different numbers of parameters used in the degradation function are very close to each other. The peak forces obtained by the hybrid model are slightly lower than those obtained by the non-hybrid model, and the non-hybrid model yields a stiffer response in the last loading stage.

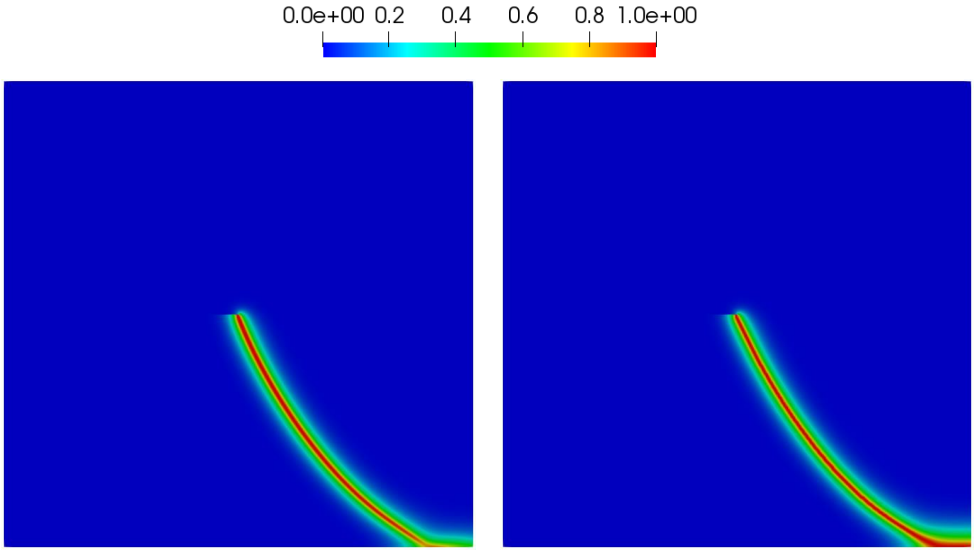


(a) Non-hybrid model (u=0.013mm) (b) Hybrid model (u=0.012mm)

Figure 4. Crack-paths of single edge notched square under shear (1 parameter used)

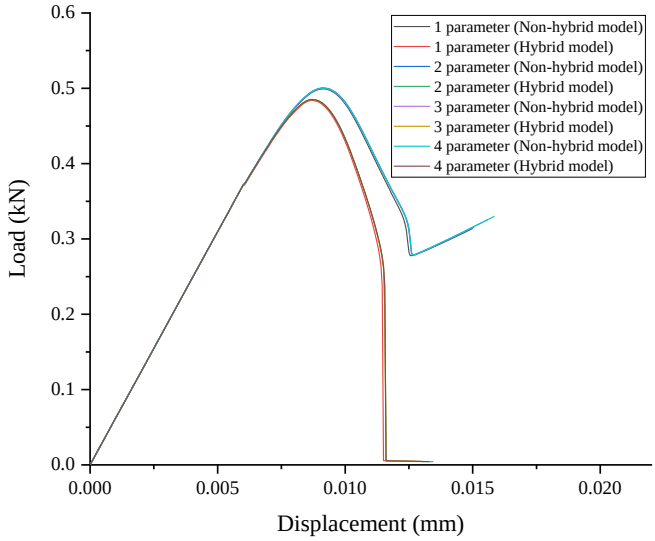


Figure 5. Load-displacement curves of single edge notched square under shear

*5.2 Three-point bending beam*

A three-point bending test on a concrete notched beam [61] is simulated in this example. The geometry and boundary conditions are shown in Figure 6(a). The material properties are: Young's modulus $E = 2.0\times10^4$ MPa, Poisson's ratio $\nu = 0.2$, failure strength $f_t = 2.4$ MPa, fracture

energy $G_c = 0.113$ N/mm.

The parameters corresponding to Cornelissen's softening law are applied and the classical phase-field model [29] is also implemented to compare the results. The mesh size in the critical zone is $h = 0.25$ mm (Figure 6(b)). Two length scales, i.e., $l_{0.} = 2.5$ and 1.25 mm, are considered in the simulation. In the algorithm with iterations, the displacement increment of $\Delta u = 10^{-4}$ mm is applied while $\Delta u = 10^{-5}$ mm is used in the algorithm without iterations.

The crack paths predicted by the phase-field are shown in Figure 7. As expected, the smaller length scale $l_0$ results in a narrower band of the crack path. The load-displacement curves computed by the classical model and the proposed model with 5 parameters in the degradation function (see Appendix A) are compared in Figure 8. It can be observed that the length scale has little influence on the load-displacement curve in the proposed model, and the results obtained by the algorithms with and without iterations are close to each other. The results obtained by the classical model are highly dependent on the value of the length scale and the peak loads are much higher than those obtained by the proposed model. The load-displacement curves obtained by the length scale $l_0$=1.25 mm with different calibrated parameters are shown in Figure 9. A good agreement can be observed between the proposed model and the experiments. Figure 9 also indicates that at least 3 parameters should be used in the model for Cornelissen's softening law to obtain accurate results.

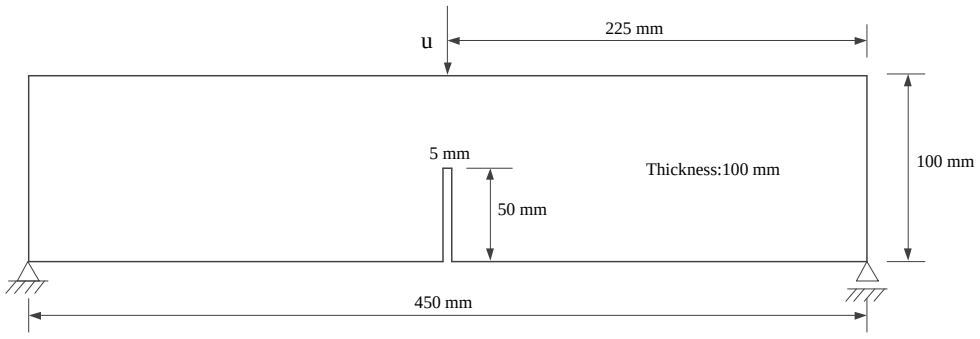


(a)

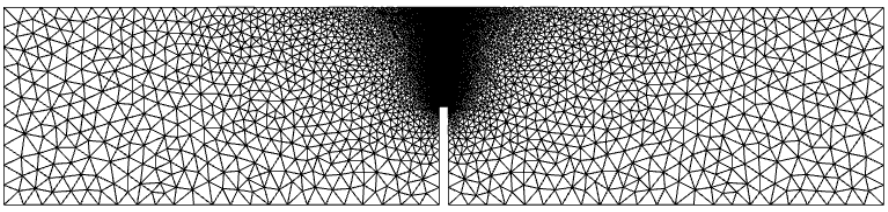

(b)

Figure 6. Geometry, boundary conditions and mesh for three-point bending beam: (a) geometry and boundary conditions; (b) mesh

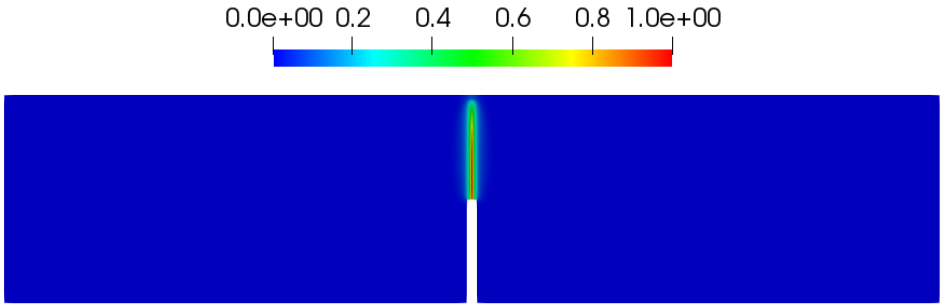


(a) Length scale =1.25mm

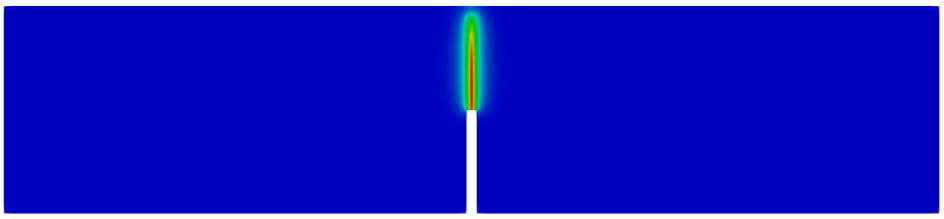

(b) Length scale =2.5mm

Figure 7. Crack-paths predicted by the proposed phase-field model (plane stress state, 1 parameter used)

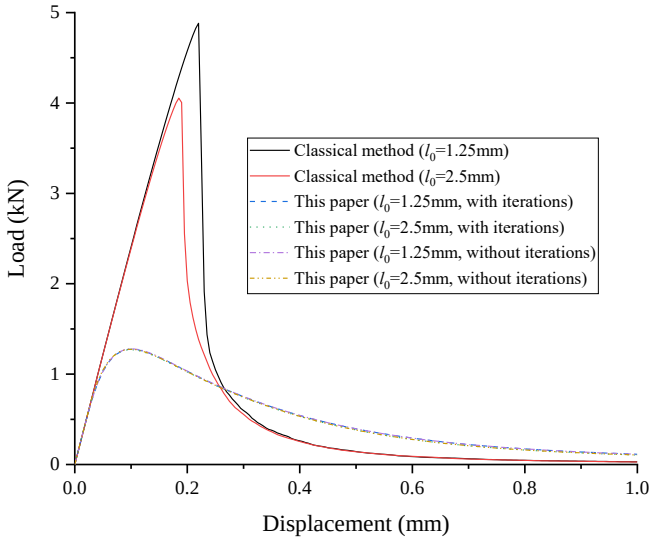


Figure 8. Load-displacement curves of the three-point bending beam (plane stress state, 1 parameter used)

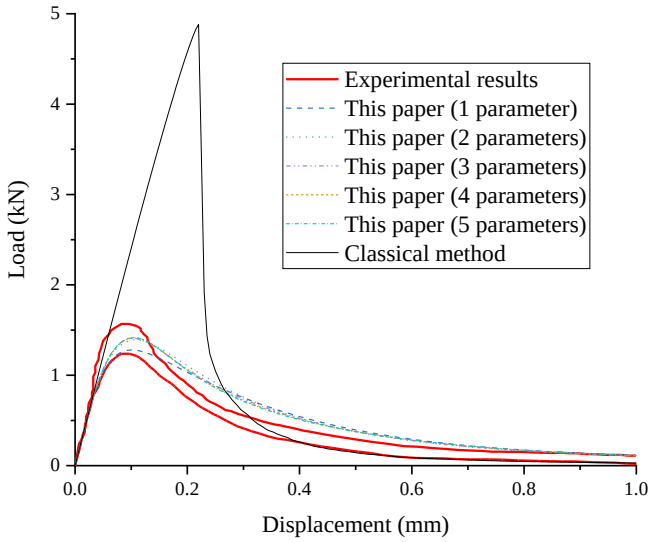


Figure 9. Load-displacement curves of the three-point bending beam (plane stress state, compared with the experimental results)

The plane strain state is also assumed and tested in this example. The crack paths are shown in Figure 10, which are similar to those obtained for the plane stress state. The comparison of the load-displacement curves between the plane stress state and the plane strain state is shown in Figure 11, and the peak forces obtained by the plane strain state are slightly higher than those obtained by the plane stress state. Figure 12 shows that the load-displacement curves obtained by the plane strain state also have a good agreement with the experimental data.

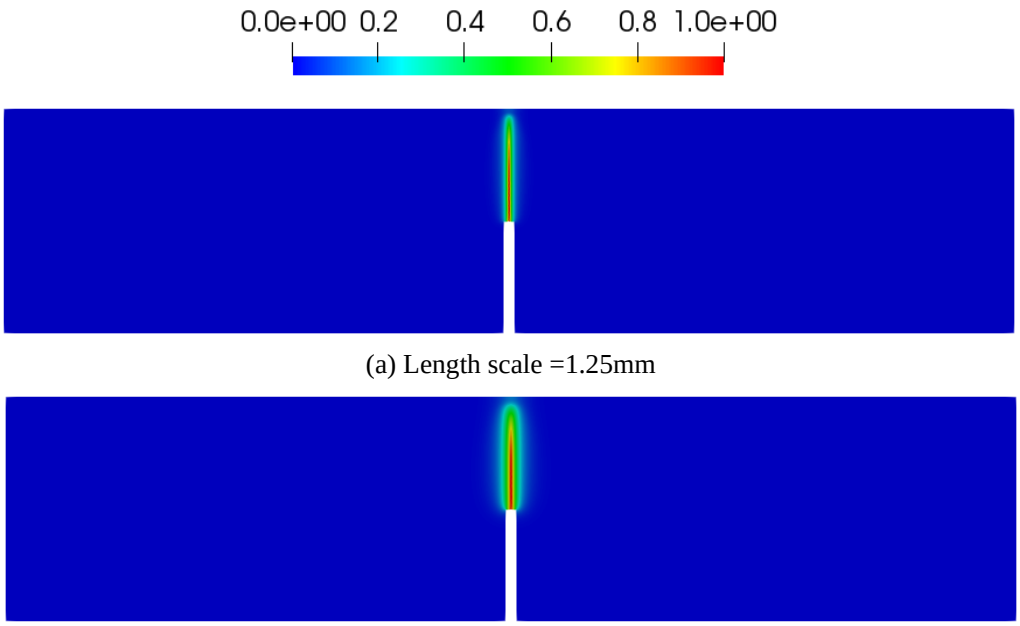


(a) Length scale =1.25mm

(b) Length scale =2.5mm

Figure 10. Crack-paths predicted by the proposed phase-field model (plane strain state, 1 parameter used)

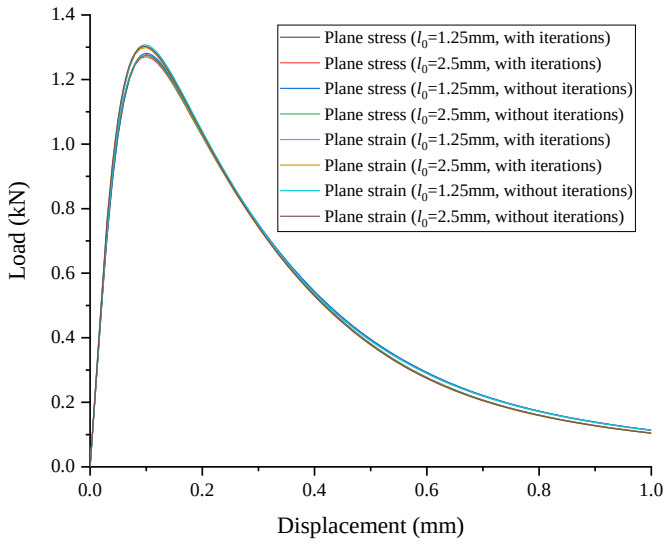


Figure 11. Load-displacement curves of the three-point bending beam (plane stress state and plane strain state, 1 parameter used)

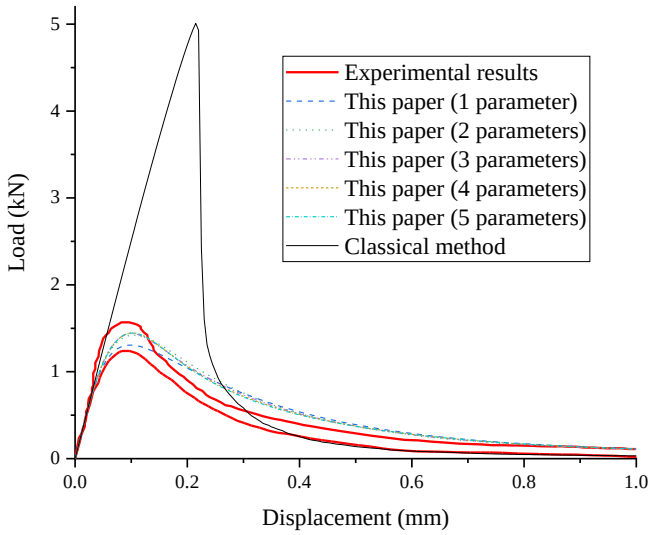


Figure 12. Load-displacement curves of the three-point bending beam (plane strain state, compared with the experimental results)

*5.3 Wedge-splitting test*

The wedge-splitting test [62] is simulated by the proposed model in this example. The geometry and boundary conditions are shown in Figure 13. The material parameters are: Young's modulus $E = 2.83\times10^4$ MPa, Poisson's ratio $\nu = 0.18$, failure strength $f_t = 2.12$ MPa, and fracture energy $G_c = 0.373$ N/mm. Two mesh sizes in the critical zone are applied to mesh the domain, i.e., $h = 1.0$ and 0.5 mm. Two length scales with $l_0 = 10$ and 5 mm are implemented in both discretizations. In the algorithm with iterations, the displacement increment of $\Delta u = 0.5\times10^{-2}$ mm is used while $\Delta u = 0.5\times10^{-3}$ mm is applied in the algorithm without iterations.

A linear softening law is applied in the simulation and the load-displacement curves obtained by the proposed model with 4 parameters (see Appendix A) are shown in Figure 14. Again, it can be observed that the results obtained by the algorithms with and without iterations are very close to each other. A slight difference can be observed from the results obtained by different length scales and mesh sizes, however, the difference is very small compared with the classical model (see Figure 15). In Figure 15, the results (without iterations) are compared with those obtained from the classical phase-field model. Again, it indicates that the proposed model has a much lower peak force and the length scale has a negligible influence on the load-displacement curve.

For the discretization with mesh size $h = 1$ mm and length scale $l_0 = 5$ mm, the

load-displacement curves obtained by both linear softening law and Cornelissen's softening law with different numbers of parameters are shown in Figure 16 and Figure 17, respectively. It can be observed that the results from both softening laws are close to the experimental results if compared with the classical phase-field model. The peak forces obtained from the linear softening law are higher than those obtained from the Cornelissen's softening law. The crack paths obtained by different softening laws and different length scales are shown in Figure 18, and similar results can be observed as in the first example.

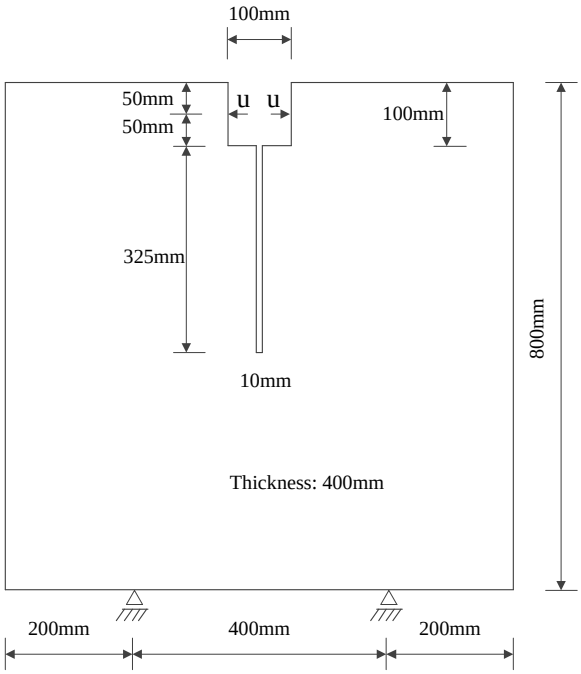


Figure 13. Geometry and boundary conditions for wedge-splitting test

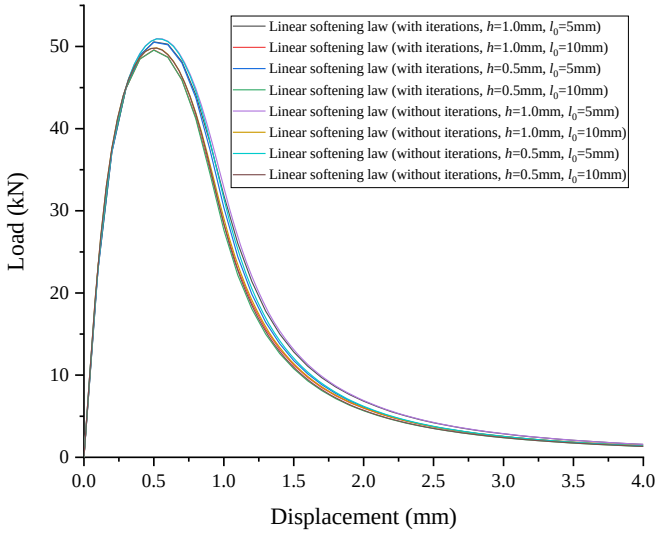

Figure 14. Load-displacement curves (algorithms with and without iterations)

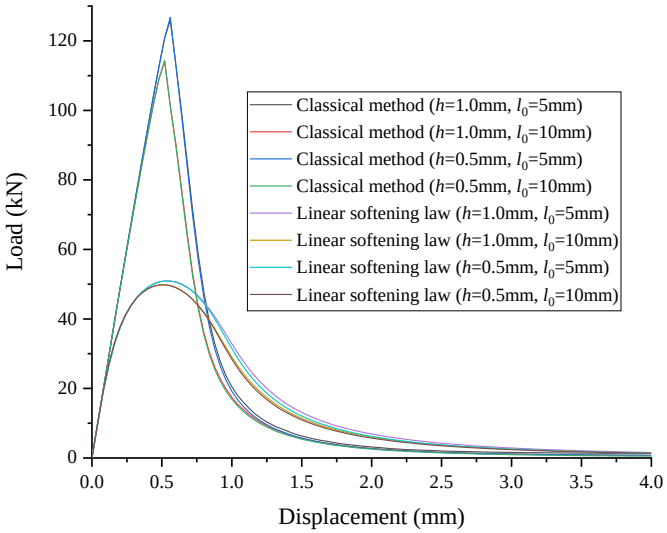


Figure 15. Load-displacement curves (compared with classical model)

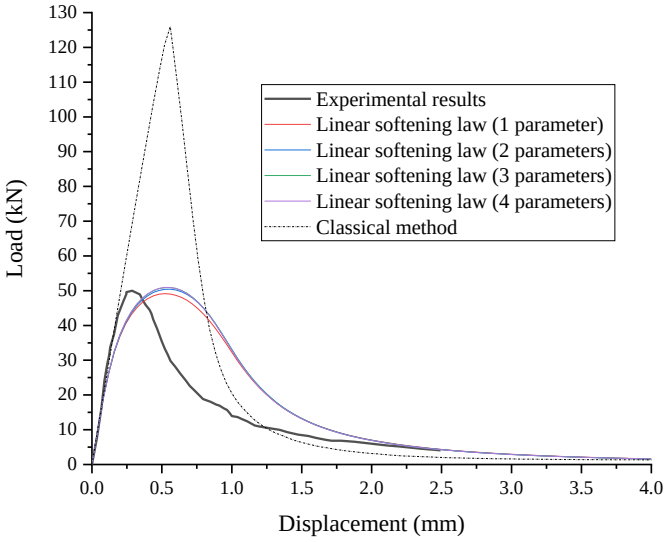


Figure 16. Load-displacement curves (linear softening law, compared with experimental results)

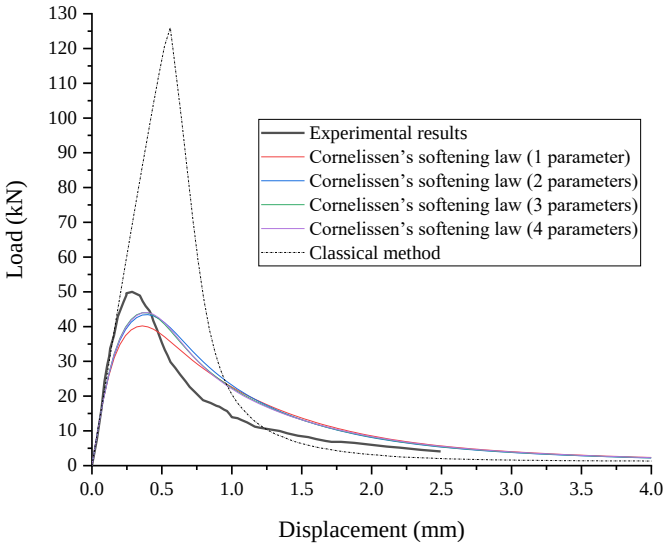


Figure 17. Load-displacement curves (Cornelissen's softening law, compared with experimental results)

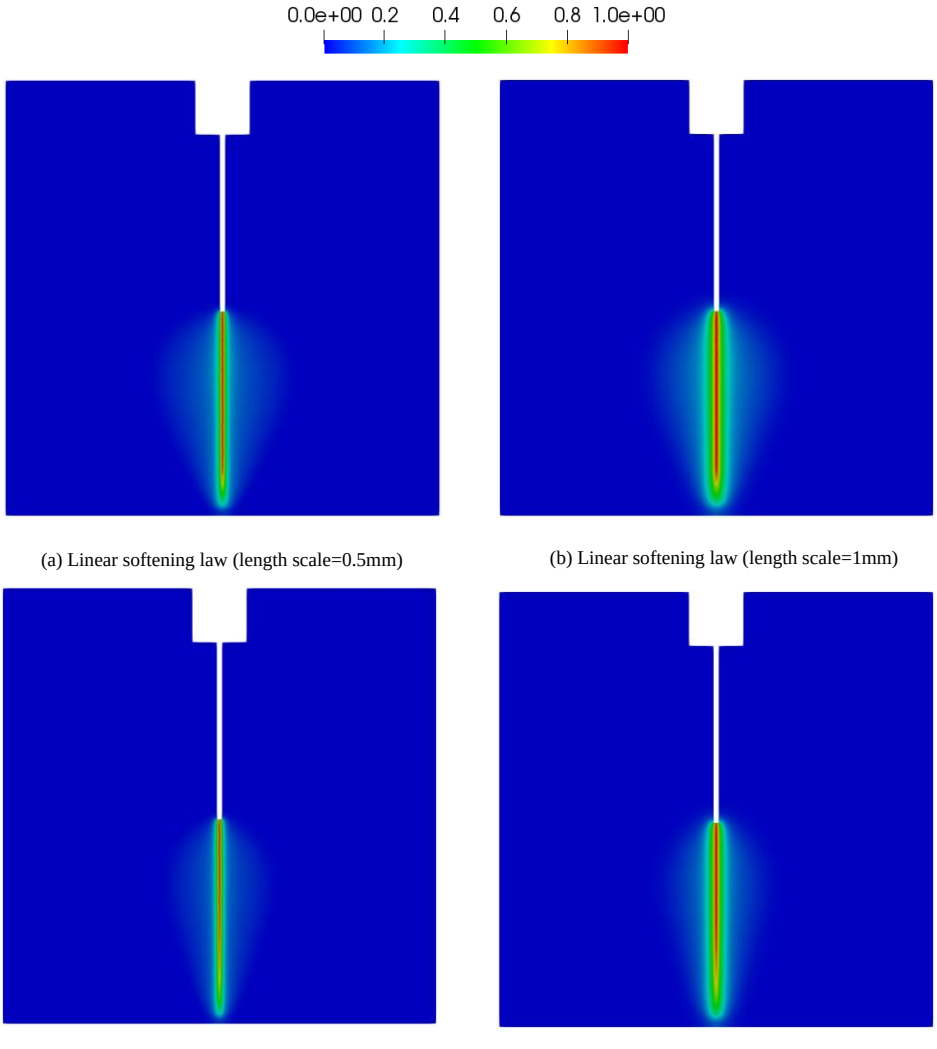


(a) Linear softening law (length scale=0.5mm)

(b) Linear softening law (length scale=1mm)

(c) Cornelissen's softening law (length scale=0.5mm)

(d) Cornelissen's softening law (length scale=1mm)

Figure 18. Crack-paths obtained by different softening laws and different length scales

*5.4 L-shaped panel*

An L-shaped panel with mixed-mode failure test [63] shown in Figure 19 is simulated in this example. The material properties are: Young's modulus $E = 2.585\times10^4$ MPa, Poisson's ratio $\nu = 0.18$, failure strength $f_t = 2.7$ MPa, fracture energy $G_c = 0.09$ N/mm. The proposed model is discretized with two mesh sizes, $h = 1.0$ and 0.5 mm in the critical zone. Two length scales $l_0 = 10$ and 5 mm are applied with the Cornelissen's softening law in the proposed phase-field model. The displacement increment of $\Delta u = 10^{-3}$ mm is used in the algorithm with iterations and $\Delta u = 10^{-4}$ mm is used in the algorithm without iterations.

The load-displacement curves obtained by the algorithms with and without iterations are shown in Figure 20, and Figure 21 compares the load-displacement curves between the proposed model and the classical model. 5 parameters are used in the degradation function in the proposed model with Cornelissen's softening law (see Appendix A). Similar results can be observed as in the former examples: 1) the algorithm without iterations can also obtain accurate results as the algorithm with iterations; 2) the length scale has a negligible influence on the load-displacement curve in the proposed model; and 3) the peak forces obtained by the proposed model are much lower than those obtained from the classical model. The load-displacement curves obtained from the mesh size $h = 1$ mm in the critical zone and the length scale $l_0 = 5$ mm are compared with the experimental results in Figure 22, and a good agreement can be observed. The crack paths obtained by the proposed model with 5 parameters are shown in Figure 23. Smooth crack paths can be observed from both simulations and the crack path in the experiment shown in Figure 19 is well captured.

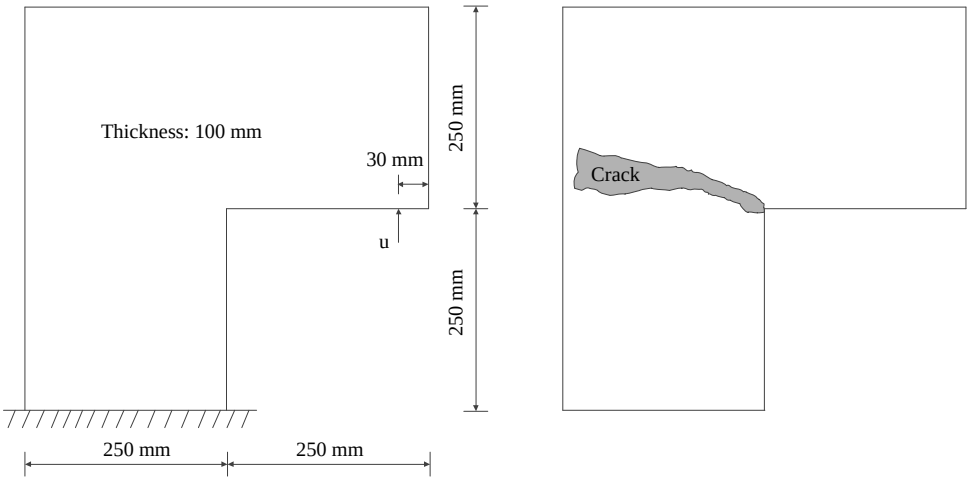


(a) Geometry and boundary conditions (b) Crack paths in experiments

Figure 19. Geometry, boundary conditions and crack paths for L-shaped panel

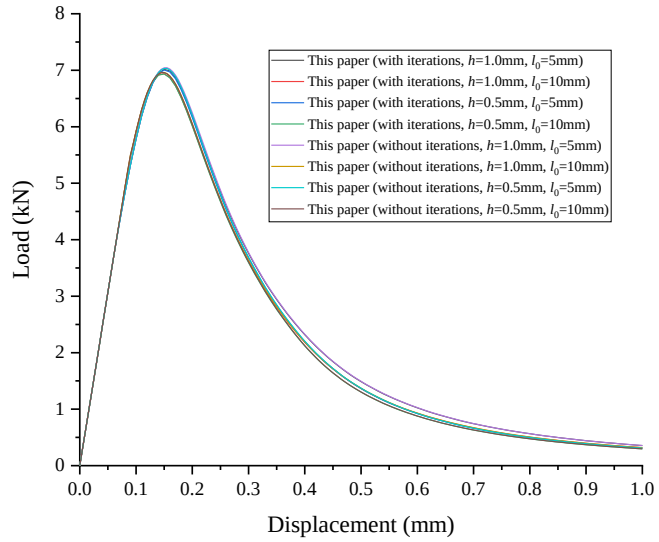


Figure 20. Load-displacement curves for L-shaped panel (Algorithms with and without iterations)

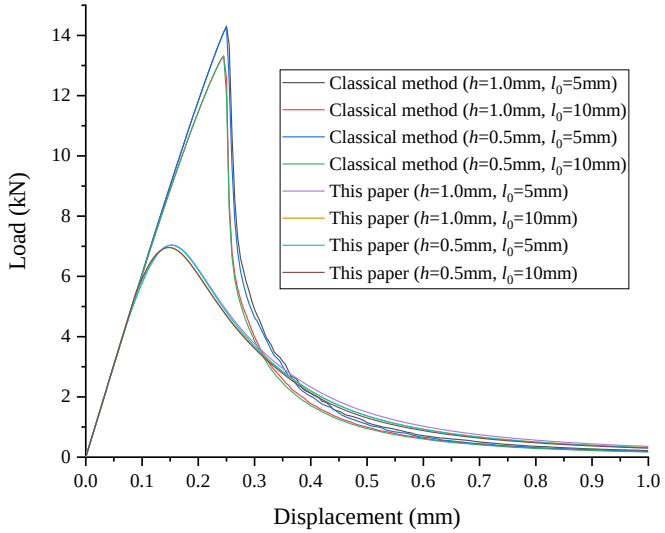


Figure 21. Load-displacement curves for L-shaped panel (Compared with classical model)

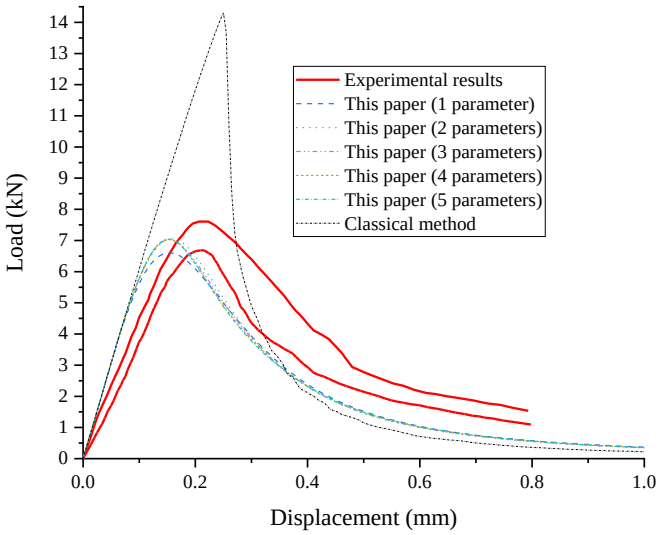


Figure 22. Load-displacement curves for L-shaped panel (Compared with experimental results)

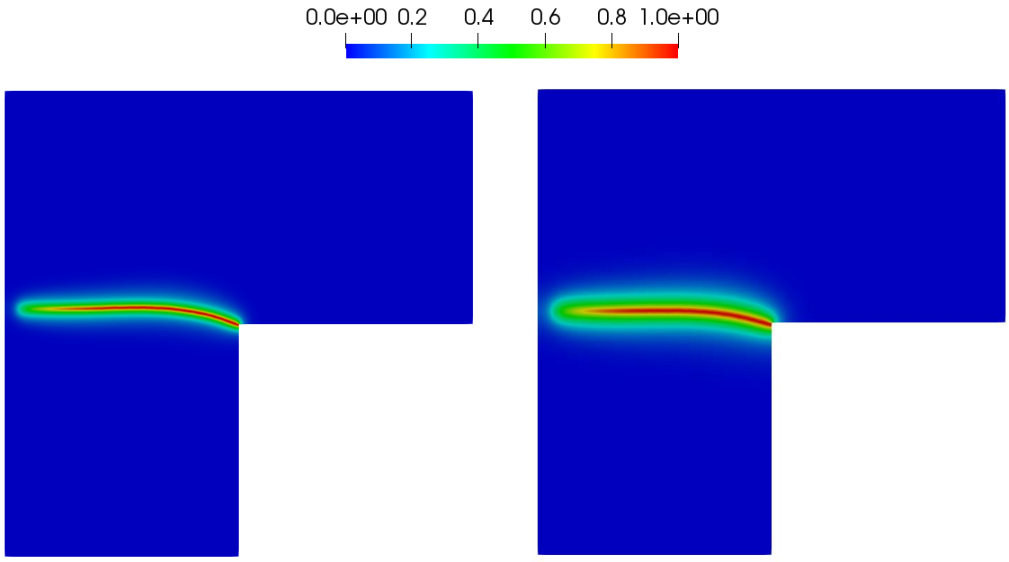


(a) Length scale =5mm (b) Length scale =10mm

Figure 23. Crack paths obtained by the proposed model (mesh size $h = 1$ mm in the critical zone)

*5.5 Asymmetrically notched beam with three holes under three-point bending*

In this example, asymmetrically notched beam with three holes shown in Figure 24 is tested, where different $e_1$ and $e_2$ are considered as: Specimen (a): $e_1 = 6$ inches and $e_2 = 1$ inch; Specimen (b): $e_1 = 5.15$ inches and $e_2 = 1.5$ inches; Specimen (c): $e_1 = 4.75$ inches and $e_2 = 1.5$ inches.

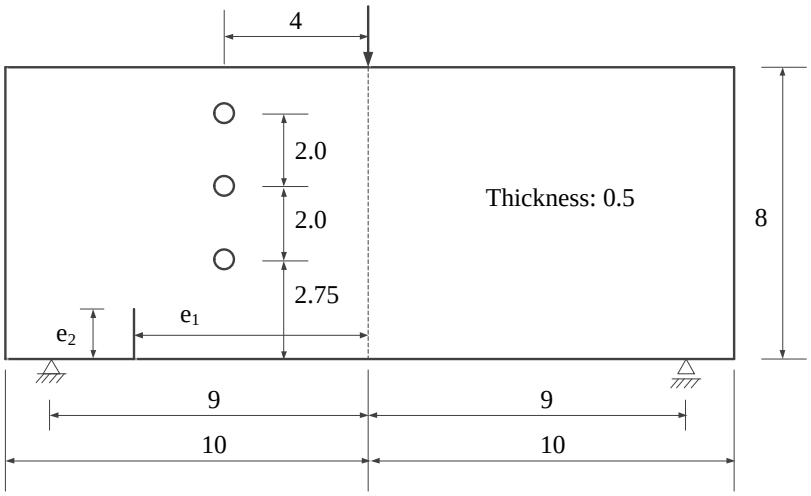


Figure 24. Asymmetrically notched beam under three-point bending (unit: inch): geometry and boundary conditions

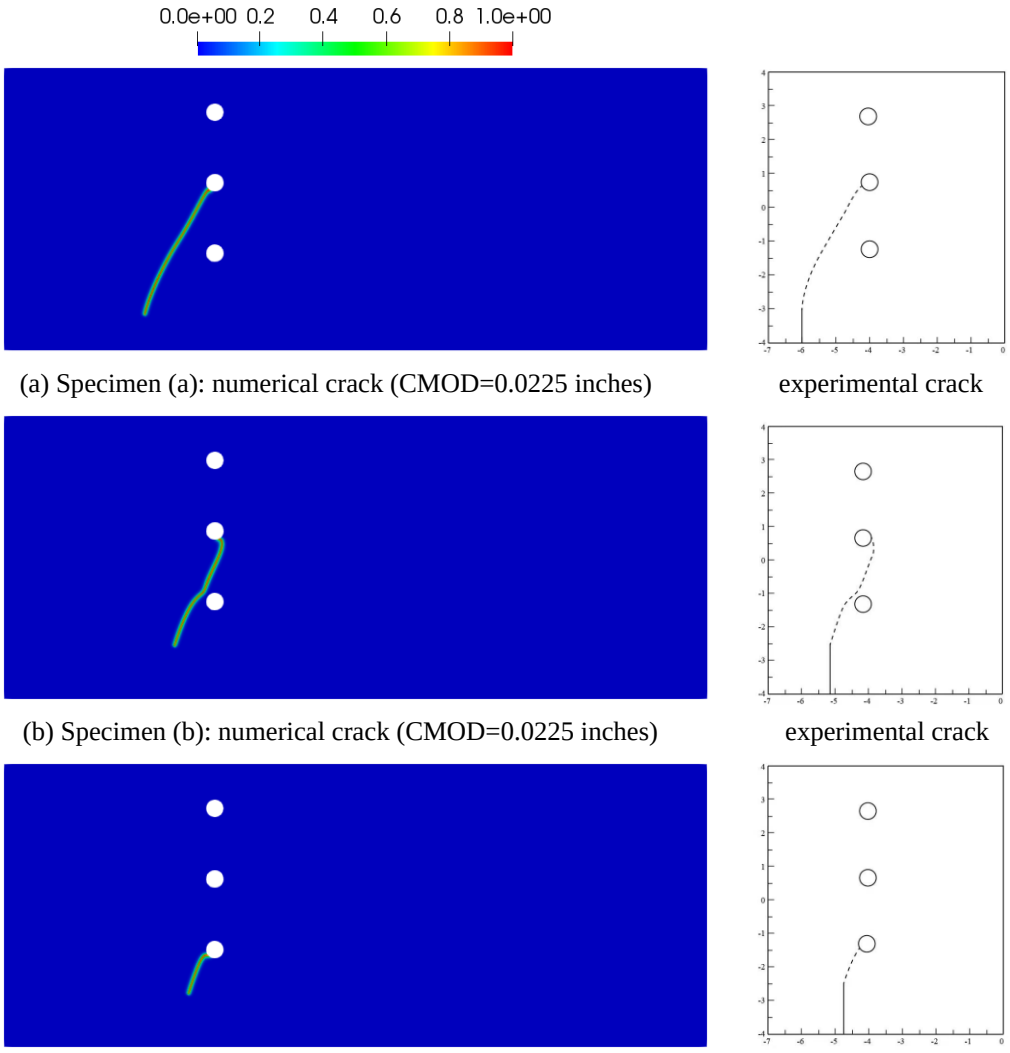


(a) Specimen (a): numerical crack (CMOD=0.0225 inches) experimental crack

(b) Specimen (b): numerical crack (CMOD=0.0225 inches) experimental crack

(c) Specimen (c): numerical crack (CMOD=0.013 inches) experimental crack

Figure 25. Crack paths for asymmetrically notched beam with three holes under three-point bending

The material properties are: Young's modulus $E = 4.75\times10^5$ psi ( $3.275\times10^3$ MPa), Poisson's ratio $\nu = 0.35$, fracture energy $G_c = 1.8$ lfb/in (315J/m$^2$) and the failure strength $f_t = 2500$ psi (17.23MPa). The fine mesh size around the critical zone is $h = 0.005$ inches and a length scale $l_0 = 0.025$ inches is applied. Linear softening law with 4 parameters is used. The crack mouth opening displacement (CMOD) based indirect displacement control [49] is employed in this example and algorithms without iterations is applied, where the increments of CMOD is $\Delta u = 10^{-5}$ inches. The crack paths obtained by the proposed method have been shown Figure 25 and they also have good agreement with the experimental results [64].

## 6. Conclusion

New phase-field model coupled with general softening law has been proposed for cohesive fracture in this work. The commonly used quadratic geometric function $\alpha(s) = s^2$ is applied in the proposed model. General softening laws in the cohesive fracture can be considered by calibrating parameters in the degradation function and an additional parameter, i.e., the failure strength, is used while calibrating. All the parameters (except for the length scale) can be obtained from the standard material properties.

The numerical examples have been compared with those obtained from the classical phase-field model and experiments. It is indicated that the length scale has a negligible influence on the global response in most cases. This is an important advantage over many other phase-field models since the global responses are highly sensitive to the length scale in these models [52, 53]. In addition, the load-displacement curves obtained from the proposed model have a good agreement with those from experimental results, which cannot be observed from the classical phase-field model. This is because an additional parameter $f_t$ is used and the proposed model can be calibrated to the special behaviour of concrete.

The contour plot of the crack phase-field shown in most figures shows a non-constant interface thickness, and the thickness at the crack tip is smaller. This indicates that the crack resistance is not everywhere the same. The Barrier method is applied to solve the bound-constrained minimization problem in this paper. Other more efficient methods may be investigated in the future. The proposed method can be applied in dynamic analysis and 3-D cases easily.

**Acknowledgments**

Financial support for the project from the National Key R&D Program of China (No. 2017YFC0404802) and National Natural Science Foundation of China (No. 51979207, No. 51609181) is acknowledged.

## Appendix A. Parameter calibration in the degradation function for general softening laws

In this appendix, the parameters in the degradation function for general softening laws are calibrated by the least squares method. The minimization problem is defined as

$$\min\{\sum_{i=1}^{N}[\sigma(s_i)-\bar{\sigma}(w_i)]^2\} \tag{57}$$

where $\sigma(s_i)$ is the numerical stress computed by Equation (30) at the $i$th phase-field $s_i \in [0,1]$, and $\bar{\sigma}(w_i)$ is the analytical stress computed by the softening laws in Equations (38) and (40) at the apparent displacement jump $w_i$, where $w_i = w(s_i)$ is computed from Equation (33). $N$ is the number of samples and $N=1000$ is used in this paper.

By solving this minimization problem, the obtained parameters are shown in Table 1. One should note that for the linear and Cornelissen's laws, the least squares method is not needed for the case with only one parameter $b_3$. Other methods for data fitting may also be applied to obtain the parameters.

Table 1. Parameters in degradation function for different softening laws

| Softening law | 1 parameter | 2 parameters | 3 parameters | 4 parameters | 5 parameters |
|---|---|---|---|---|---|
| Linear softening | $b_3$=-0.594715 | $b_3$=-0.874311, $b_4$=0.279595 | $b_3$=-1.145932, $b_4$=0.984587, $b_5$=-0.433370 | $b_3$=-1.267684, $b_4$=1.606410, $b_5$=-1.413509, $b_6$=0.480067 | $b_3$=-1.377677, $b_4$=2.470444, $b_5$=-3.728645, $b_6$= 3.030202, $b_7$= -0.989039 |
| Cornelissen's softening | $b_3$=1.6728 | $b_3$=-0.02810, $b_4$=1.700900 | $b_3$=-1.295829, $b_4$=6.195769, $b_5$=-3.227140 | $b_3$=-0.236056, $b_4$=-1.267581, $b_5$=11.785838, $b_6$=-8.609402 | $b_3$=-0.868397, $b_4$=5.499320, $b_5$=-12.007010, $b_6$= 24.216320, $b_7$= -15.167433 |

## References

[1] A.A. Griffith and M. Eng, *VI. The phenomena of rupture and flow in solids.* Phil. Trans. R. Soc. Lond. A, 1921. **221**(582-593): 163-198.

[2] T.L. Anderson, *Fracture mechanics: fundamentals and applications*. 2017: CRC press.

[3] G.I. Barenblatt, *The formation of equilibrium cracks during brittle fracture. General ideas and*

*hypotheses. Axially-symmetric cracks.* Journal of Applied Mathematics and Mechanics, 1959. **23**(3): 622-636.

[4] A. Hillerborg, M. Modéer, and P.-E. Petersson, *Analysis of crack formation and crack growth in concrete by means of fracture mechanics and finite elements.* Cement and concrete research, 1976. **6**(6): 773-781.

[5] G. Zi and T. Belytschko, *New crack‐tip elements for XFEM and applications to cohesive cracks.* International Journal for Numerical Methods in Engineering, 2003. **57**(15): 2221-2240.

[6] J.-H. Lv, Y.-Y. Jiao, P. Wriggers, T. Rabczuk, X.-T. Feng, and F. Tan, *Efficient integration of crack singularities in the extended finite element method: Duffy-distance transformation and conformal preconditioning strategy.* Computer Methods in Applied Mechanics and Engineering, 2018. **340**: 559-576.

[7] T. Cruse, *Boundary-Integral Equation Method for Three-Dimensional Elastic Fracture Mechanics Analysis*, 1975, PRATT AND WHITNEY AIRCRAFT EAST HARTFORD CONN.

[8] T. Belytschko, L. Gu, and Y. Lu, *Fracture and crack growth by element free Galerkin methods.* Modelling and Simulation in Materials Science and Engineering, 1994. **2**(3A): 519.

[9] H. Ren, X. Zhuang, and T. Rabczuk, *Dual-horizon peridynamics: A stable solution to varying horizons.* Computer Methods in Applied Mechanics and Engineering, 2017. **318**: 762-782.

[10] H. Ren, X. Zhuang, Y. Cai, and T. Rabczuk, *Dual-horizon Peridynamics.* International Journal for Numerical Methods in Engineering, 2016. **108**(12): 1451-1476.

[11] T. Rabczuk, G. Zi, S. Bordas, and H. Nguyen-Xuan, *A simple and robust three-dimensional cracking-particle method without enrichment.* Computer Methods in Applied Mechanics & Engineering, 2010. **199**(37): 2437-2455.

[12] T. Rabczuk and T. Belytschko, *Cracking particles: A simplified meshfree method for arbitrary evolving cracks.* International Journal for Numerical Methods in Engineering, 2010. **61**(13): 2316-2343.

[13] P. Areias, J. Reinoso, P.P. Camanho, J.C.D. Sá, and T. Rabczuk, *Effective 2D and 3D crack propagation with local mesh refinement and the screened Poisson equation.* Engineering Fracture Mechanics, 2017. **189**: S0013794417307804.

[14] P. Areias, M.A. Msekh, and T. Rabczuk, *Damage and fracture algorithm using the screened Poisson equation and local remeshing.* Engineering Fracture Mechanics, 2016. **158**: 116-143.

[15] Y. Fei, X.T. Feng, J.H. Lv, P.Z. Pan, and S.J. Li, *Continuous-discontinuous cellular automaton method for cohesive crack growth in rock.* Engineering Fracture Mechanics, 2017. **188**: S0013794417306276.

[16] F. Yan, P.-Z. Pan, X.-T. Feng, S.-J. Li, and Q. Jiang, *A novel fast overrelaxation updating method for continuous-discontinuous cellular automaton.* Applied Mathematical Modelling, 2019. **66**: 156-174.

[17] M. Ambati, T. Gerasimov, and L. De Lorenzis, *A review on phase-field models of brittle fracture and a new fast hybrid formulation.* Computational Mechanics, 2015. **55**(2): 383-405.

[18] I. Aranson, V. Kalatsky, and V. Vinokur, *Continuum field description of crack propagation.* Physical Review Letters, 2000. **85**(1): 118.

[19] A. Karma, D.A. Kessler, and H. Levine, *Phase-field model of mode III dynamic fracture.* Physical Review Letters, 2001. **87**(4): 045501.

[20] V. Hakim and A. Karma, *Laws of crack motion and phase-field models of fracture.* Journal of the Mechanics and Physics of Solids, 2009. **57**(2): 342-368.

[21] R. Spatschek, E. Brener, and A. Karma, *Phase field modeling of crack propagation.* Philosophical Magazine, 2011. **91**(1): 75-95.

[22] H. Henry and H. Levine, *Dynamic instabilities of fracture under biaxial strain using a phase field model.* Physical review letters, 2004. **93**(10): 105504.

[23] C.-H. Chen, E. Bouchbinder, and A. Karma, *Instability in dynamic fracture and the failure of the classical theory of cracks.* Nature Physics, 2017. **13**(12): 1186.

[24] H. Amor, J.-J. Marigo, and C. Maurini, *Regularized formulation of the variational brittle fracture with unilateral contact: Numerical experiments.* Journal of the Mechanics and Physics of Solids, 2009. **57**(8): 1209-1229.

[25] C. Kuhn and R. Müller, *A continuum phase field model for fracture.* Engineering Fracture Mechanics, 2010. **77**(18): 3625-3634.

[26] G.A. Francfort and J.-J. Marigo, *Revisiting brittle fracture as an energy minimization problem.* Journal of the Mechanics and Physics of Solids, 1998. **46**(8): 1319-1342.

[27] B. Bourdin, G.A. Francfort, and J.-J. Marigo, *Numerical experiments in revisited brittle fracture.* Journal of the Mechanics and Physics of Solids, 2000. **48**(4): 797-826.

[28] C. Miehe, F. Welschinger, and M. Hofacker, *Thermodynamically consistent phase‐field models of fracture: Variational principles and multi‐field FE implementations.* International Journal for Numerical Methods in Engineering, 2010. **83**(10): 1273-1311.

[29] C. Miehe, M. Hofacker, and F. Welschinger, *A phase field model for rate-independent crack propagation: Robust algorithmic implementation based on operator splits.* Computer Methods in Applied Mechanics and Engineering, 2010. **199**(45): 2765-2778.

[30] C.J. Larsen, C. Ortner, and E. Süli, *Existence of solutions to a regularized model of dynamic fracture.* Mathematical Models and Methods in Applied Sciences, 2010. **20**(07): 1021-1048.

[31] B. Bourdin, C.J. Larsen, and C.L. Richardson, *A time-discrete model for dynamic fracture based on crack regularization.* International journal of fracture, 2011. **168**(2): 133-143.

[32] M.J. Borden, C.V. Verhoosel, M.A. Scott, T.J. Hughes, and C.M. Landis, *A phase-field description of dynamic brittle fracture.* Computer Methods in Applied Mechanics and Engineering, 2012. **217**: 77-95.

[33] M. Hofacker and C. Miehe, *Continuum phase field modeling of dynamic fracture: variational principles and staggered FE implementation.* International Journal of Fracture, 2012. **178**(1-2): 113-129.

[34] M. Hofacker and C. Miehe, *A phase field model of dynamic fracture: Robust field updates for the analysis of complex crack patterns.* International Journal for Numerical Methods in Engineering, 2013. **93**(3): 276-301.

[35] A. Schlüter, A. Willenbücher, C. Kuhn, and R. Müller, *Phase field approximation of dynamic brittle fracture.* Computational Mechanics, 2014. **54**(5): 1141-1161.

[36] H.L. Ren, X.Y. Zhuang, C. Anitescu, and T. Rabczuk, *An explicit phase field method for brittle dynamic fracture.* Computers & Structures, 2019. **217**: 45-56.

[37] F. Amiri, D. Millán, Y. Shen, T. Rabczuk, and M. Arroyo, *Phase-field modeling of fracture in linear thin shells.* Theoretical and Applied Fracture Mechanics, 2014. **69**: 102-109.

[38] P. Areias, T. Rabczuk, and M.A. Msekh, *Phase-field analysis of finite-strain plates and shells including element subdivision.* Computer Methods in Applied Mechanics and Engineering, 2016. **312**: 322-350.

[39] M.A. Msekh, N.H. Cuong, G. Zi, P. Areias, X. Zhuang, and T. Rabczuk, *Fracture properties*

*prediction of clay/epoxy nanocomposites with interphase zones using a phase field model.* Engineering Fracture Mechanics, 2018. **188**: 287-299.

[40] B. Chen, Y. Sun, B.R. Barboza, A.R. Barron, and C. Li, *Phase-field simulation of hydraulic fracturing with a revised fluid model and hybrid solver.* Engineering Fracture Mechanics, 2020. **229**: 106928.

[41] J.-Y. Wu, *A unified phase-field theory for the mechanics of damage and quasi-brittle failure.* Journal of the Mechanics and Physics of Solids, 2017. **103**: 72-99.

[42] C.V. Verhoosel and R. de Borst, *A phase‐field model for cohesive fracture.* International Journal for numerical methods in Engineering, 2013. **96**(1): 43-62.

[43] J. Vignollet, S. May, R. De Borst, and C.V. Verhoosel, *Phase-field models for brittle and cohesive fracture.* Meccanica, 2014. **49**(11): 2587-2601.

[44] S. May, J. Vignollet, and R. De Borst, *A numerical assessment of phase-field models for brittle and cohesive fracture: Γ-convergence and stress oscillations.* European Journal of Mechanics-A/Solids, 2015. **52**: 72-84.

[45] S. Conti, M. Focardi, and F. Iurlano. *Phase field approximation of cohesive fracture models*. in *Annales de l'Institut Henri Poincare (C) Non Linear Analysis*. 2016. Elsevier.

[46] R. Alessi, J.-J. Marigo, C. Maurini, and S. Vidoli, *Coupling damage and plasticity for a phase-field regularisation of brittle, cohesive and ductile fracture: one-dimensional examples.* International Journal of Mechanical Sciences, 2018. **149**: 559-576.

[47] V.P. Nguyen and J.-Y. Wu, *Modeling dynamic fracture of solids with a phase-field regularized cohesive zone model.* Computer Methods in Applied Mechanics and Engineering, 2018. **340**: 1000-1022.

[48] J.-Y. Wu, *A geometrically regularized gradient-damage model with energetic equivalence.* Computer Methods in Applied Mechanics and Engineering, 2018. **328**: 612-637.

[49] J.-Y. Wu, *Robust numerical implementation of non-standard phase-field damage models for failure in solids.* Computer Methods in Applied Mechanics and Engineering, 2018.

[50] J.-Y. Wu and V.P. Nguyen, *A length scale insensitive phase-field damage model for brittle fracture.* Journal of the Mechanics and Physics of Solids, 2018. **119**: 20-42.

[51] D.-C. Feng and J.-Y. Wu, *Phase-field regularized cohesive zone model (CZM) and size effect of concrete.* Engineering Fracture Mechanics, 2018. **197**: 66-79.

[52] F. Freddi and F. Iurlano, *Numerical insight of a variational smeared approach to cohesive fracture.* Journal of the Mechanics and Physics of Solids, 2017. **98**: 156-171.

[53] J.M. Sargado, E. Keilegavlen, I. Berre, and J.M. Nordbotten, *High-accuracy phase-field models for brittle fracture based on a new family of degradation functions.* Journal of the Mechanics and Physics of Solids, 2018. **111**: 458-489.

[54] C. Kuhn, A. Schlüter, and R. Müller, *On degradation functions in phase field fracture models.* Computational Materials Science, 2015. **108**: 374-384.

[55] X. Zhang, C. Vignes, S.W. Sloan, and D. Sheng, *Numerical evaluation of the phase-field model for brittle fracture with emphasis on the length scale.* Computational Mechanics, 2017. **59**(5): 737-752.

[56] K. Pham, H. Amor, J.-J. Marigo, and C. Maurini, *Gradient damage models and their use to approximate brittle fracture.* International Journal of Damage Mechanics, 2011. **20**(4): 618-652.

[57] J.-Y. Wu, V.P. Nguyen, C.T. Nguyen, D. Sutula, S. Bordas, and S. Sinaie, *Phase field modeling of*

*fracture.* Advances in Applied Mechancis: Multi-scale Theory and Computation, 2019. **53**.

[58] G. Lancioni and G. Royer-Carfagni, *The variational approach to fracture mechanics. A practical application to the French Panthéon in Paris.* Journal of elasticity, 2009. **95**(1-2): 1-30.

[59] J.-Y. Wu and M. Cervera, *A novel positive/negative projection in energy norm for the damage modeling of quasi-brittle solids.* International Journal of Solids and Structures, 2018. **139-140**: 250-269.

[60] H. Cornelissen, D. Hordijk, and H. Reinhardt, *Experimental determination of crack softening characteristics of normalweight and lightweight.* Heron, 1986. **31**(2): 45.

[61] J.G. Rots, *Computational modeling of concrete fracture.* 1988.

[62] B.G. Trunk, *Einfluss der Bauteilgrösse auf die Bruchenergie von Beton*, 1999, ETH Zurich.

[63] B.J. Winkler, *Traglastuntersuchungen von unbewehrten und bewehrten Betonstrukturen auf der Grundlage eines objektiven Werkstoffgesetzes für Beton*. 2001: Innsbruck University Press.

[64] A.R. Ingraffea and M. Grigoriu, *Probabilistic fracture mechanics: A validation of predictive capability*, 1990, CORNELL UNIV ITHACA NY DEPT OF STRUCTURAL ENGINEERING.